



IVIM-DKI with parametric reconstruction method for lymph node evaluation and characterization in lymphoma: A preliminary study comparison with FDG-PET/CT

Archana Vadiraj Malagi ^a, Devasenathipathy Kandasamy ^b, Deepam Pushpam ^c, Kedar Khare ^d, Raju Sharma ^b, Rakesh Kumar ^e, Sameer Bakhshi ^c, Amit Mehndiratta ^{a,f,*}

^a Centre for Biomedical Engineering, Indian Institute of Technology Delhi, New Delhi, India

^b Department of Radio Diagnosis, All India Institute of Medical Sciences, New Delhi, India

^c Department of Medical Oncology, All India Institute of Medical Sciences, New Delhi, India

^d Department of Physics, Indian Institute of Technology Delhi, New Delhi, India

^e Department of Nuclear Medicine, All India Institute of Medical Sciences, New Delhi, India

^f Department of Biomedical Engineering, All India Institute of Medical Sciences, New Delhi, India



ARTICLE INFO

Keywords:

Diffusion kurtosis imaging
Diffusion-weighted imaging
Hodgkin lymphoma
Intravoxel incoherent motion
Non-hodgkin lymphoma
Total variation penalty function

ABSTRACT

To investigate IVIM-DKI in diagnosing benign and malignant lymph nodes in lymphoma and its subtypes in comparison to FDG-PET/CT. A total of twenty-one ($n = 21$) patients diagnosed with biopsy-proven Hodgkin lymphoma(HL; $n = 13$) and non-Hodgkin lymphoma (NHL; $n = 8$) were prospectively evaluated. All patients underwent MRI(T1-weighted, Short-Tau-Inversion-Recovery (STIR)), and IVIM-DKI was acquired with 9b-values (0–2000s/mm²) at 1.5T and whole-body FDG-PET/CT. The maximum and average standard uptake values (SUV_{max} and SUV_{mean}) were calculated using PET images. IVIM-DKI parameters (diffusion coefficient(D), pseudo-diffusion coefficient (D*), perfusion fraction (f), and kurtosis (k)) were estimated using IVIM-DKI model with total variation (TV) method (IDTV model). Area-under-curve from receiver-operating-curve (ROC) analysis was used to examine diagnostic value of IVIM-DKI parameters in differentiation between benign and malignant lymph nodes and HL from NHL. Machine learning-based classification of histogram features were performed using linear classifier model. For malignant vs. benign lymph nodes, apparent diffusion coefficient (ADC), f, and k were significantly ($p < 0.05$) lower in malignant vs. benign lymph nodes. f (AUC:0.88) and k (AUC:0.83) showed high AUC and histogram features combination of f (variance + skewness + kurtosis) showed highest accuracy of 97.2% and AUC of 1. ADC, D, D*, and f were significantly ($p < 0.05$) lower in NHL than HL. D* showed highest AUC of 0.85 than D (AUC:0.84), ADC (AUC:0.84), and f (AUC:0.74) in NHL vs. HL. SUV_{max} (spearman-rho = 0.85), ADC (spearman-rho = 0.50), D (spearman-rho = 0.48), and D* (spearman-rho = 0.49) showed significant ($p < 0.05$) positive correlation with SUV_{mean}. Multi-b-values IVIM-DKI with histogram analysis helps characterize benign and malignant lymph nodes in lymphomas. IVIM-DKI parameters can differentiate malignant lymph nodes in HL and NHL superior to PET parameters.

1. Introduction

Lymphoma is a lymphoproliferative disease characterized by the proliferation of B-cells, T-cells, and natural killer lymphocytes. Most common types of lymphoma consist of non-Hodgkin lymphoma (NHL), with diffuse large B-cell lymphoma (DLBCL) and follicular lymphoma accounting for 80–85% of NHL, and classical Hodgkin lymphoma (HL), about 88% of HL [1]. Understanding the anatomical distribution of this

cancer throughout the body after diagnosis is a crucial aspect of its treatment. Thus, imaging modality can provide accurate diagnosis and staging of lymph node metastases, and differentiation of benign and malignant lymph nodes; thereby optimizing the lymphoma treatment regime. Current standards in clinical diagnosis of lymphoma includes, fluorodeoxyglucose-PET (FDG-PET), computed tomography (CT), and FDG-PET/CT [2]. Contrast-enhanced CT can detect lymph nodes and can be used to determine treatment response [3]. Nevertheless, malignancy

* Corresponding author. Centre for Biomedical Engineering, Indian Institute of Technology Delhi, Hauz Khas, New Delhi, 110016, India.

E-mail address: amit.mehndiratta@keble.oxon.org (A. Mehndiratta).

in small lymph nodes is difficult to identify with CT [4]. While FDG-PET/CT is used as a clinical routine to find the exact location of the lesion, describing what it looks like, and evaluate the treatment response [5,6]. The main disadvantage of PET, CT or PET/CT is radiation exposure which might initiate secondary tumor growth and poor detection rate of the small and extranodal lymph nodes involved in lymphoma [7]. PET or CT scans are often performed at the beginning of treatment and during therapy to assess the patient's response to therapy. Therefore, it would be beneficial to promote non-invasive and radiation-free imaging, such as MRI diffusion-weighted imaging (DWI).

DWI provides function information about the tumor environment and has recently shown promise in lymph node characterization [8], staging, and treatment response [9]. DWI is a non-invasive imaging modality that captures microscopic water molecule motion with the Gaussian assumption of water distribution. However, a non-Gaussian model of water diffusion has been shown to accurately detect tumor heterogeneity using intravoxel incoherent motion with diffusion kurtosis imaging (IVIM-DKI) [10].

IVIM-DKI not only provides diffusion and perfusion information but also provides the kurtosis (k) measure of the tissue [10,11]. However, IVIM-DKI analysis using the standard IVIM-DKI model generates high spurious values and thus produces noisy parametric maps [12]. Recently, precise parameter estimation with a superior-quality parametric map in IVIM-DKI analysis has been generated with parametric map reconstruction methods such as the total variation (TV) penalty function. This IVIM-DKI model with the TV method to adaptively remove any non-physiological inhomogeneity in parameter maps by removing spurious values. TV method is effective in lymphoma [13] and additionally in various cancer applications such as Ewing sarcoma [14], osteosarcoma [14–16], prostate cancer [12,17], and pancreatic masses [18].

Studies involving IVIM and DKI analysis in oncological imaging of the brain, breast, liver, kidney, prostate, orbital, and head and neck, etc. have shown promising results in detection, characterization, evaluation, and the prediction of treatment response [19–24]. There is limited literature on the detection and characterization of benign and malignant lymph nodes in lymphoma utilizing IVIM-DKI, mostly focused on head and neck cancer [10,25,26]. Histogram analysis of parameters is known to capture the heterogeneity and progression of tumor [27]. IVIM-DKI with TV model and texture analysis has shown to improve classification of pancreatic masses in a recent study [18]. Additionally, there have been no studies on the characterization of lymphoma subtypes using IVIM-DKI analysis with the TV method. Thus, this study aimed to investigate the role of quantitative parameters such as diffusion coefficient (D), pseudo-diffusion coefficient (D^*), perfusion fraction (f), and kurtosis (k) obtained from the multi-b-values IVIM-DKI model with the TV method for the characterization of malignant lymphoma subtypes such as HL and NHL in comparison with PET imaging. This study also aimed to assess the added value of histogram analysis of the IVIM-DKI parameters in differentiation of lesions in lymph nodes. Furthermore, to examine the role of IVIM-DKI in the assessment of malignant lymphoma subtypes.

2. Materials and methods

2.1. Clinical data characteristics

The institutional ethics board approved this prospective single-center investigation with patient enrollment after the written informed consent. This study's inclusion criteria comprised treatment-naïve individuals with biopsy-proven lymphoma. The patient's age was in the range of 18–70 years old. Exclusion criteria included: recurrent disease following previously successful treatment, prior anti-tumor therapy for lymphoma, uncooperative patients, patients requiring general anesthesia for MRI, and MRI contraindications (such as claustrophobia or pacemaker). From June 2019 to December 2020,

patients with lymphoma who were histologically-proven by excision biopsy were enrolled for the MRI and FDG-PET/CT acquisition. Based on inclusion criteria, 30 patients were included in this study. However, owing to incomplete scans ($n = 5$), and poor image quality ($n = 4$), total 9 patient data were excluded from further analysis. Finally, the dataset of 21 patients was included in the analysis under this investigation (Age (mean \pm SD): 34 ± 11.4 years old, Female/Male: 4/17). All MRI and FDG-PET/CT scans were performed 1–2 weeks before the initiation of treatment. As indicated in Table 1, histopathological results revealed that the number of patients diagnosed with HL, DLBCL, and follicular lymphoma was 13, 5, and 3, respectively. Ann Arbor staging was conducted before therapy and was based on PET/CT and biopsy results, with the number of patients in stage IV, stage III, stage II, and stage I were 9, 8, 2, and 2, respectively.

The identified malignant lymph nodes were biopsy-proven or validated on PET/CT imaging for tumor location with significant FDG uptake. While benign nodes were chosen based on small lymph nodes (less than 1 cm in the short axis) with hyperintensity on baseline IVIM-DKI imaging ($b = 0$ s/mm 2) and validated by PET/CT as the gold standard approach with no FDG uptake in the corresponding region.

2.2. Imaging protocol

2.2.1. MRI and IVIM-DKI protocol

All patients were scanned with 1.5 T MRI (Achieva; Philips Healthcare, Best, the Netherlands). Short-TI Inversion Recovery (STIR) was acquired with turbo spin echo, scanning mode: inversion recovery, (Thoracic: TR = 1.503s and TE = 0.09s; Abdomen: TR = 1.503s and TE = 0.06s). Thoracic and abdominal region: FOV, RL (mm) 400; AP (mm) = 283; FH (mm) = 402; and ACQ voxel size, RL (mm) = 1.55; AP (mm) = 1.75; Slice thickness (mm) = 6 with zero slice gap. Reconstruction voxel size, RL (mm) = 1.39; AP (mm) = 1.39; Total no. of slices: 67; Reconstruction matrix: 288.

Multi-b-value DWI dataset for IVIM-DKI was collected with single-shot echo planar imaging with 9 b-values (number of averages) = 0 (1), 35 (1), 50 (1), 100 (1), 175 (1), 300 (1), 500 (1), 1500 (2), 2000 (2) s/mm 2 using phased-array surface coil for the thoracic and abdominal regions (Thoracic and abdomen: TR = 12.44s, TE = 0.081s). The choice of b-values was based on previous literature [17,26]. ACQ voxel size is RL (mm) = 3; AP (mm) = 3; Slice thickness (mm) = 6 with zero slice gap. Total number of slices: 67; reconstruction matrix: 192; reconstruction voxel size, RL (mm) = 2.1875; AP (mm) = 2.1875; total number of slices: 67; reconstruction matrix: 192. The total scan duration to acquire multi-b-value DWI was 12 min. A representative image of multi-b-value DWI at different b-values of a 28-year-old female patient suffering from classical Hodgkin lymphoma (HL), Nodular Sclerosis type at stage IV is presented in Supplementary Material Fig. S1.

2.2.2. FDG-PET/CT protocol

PET/CT examinations were performed with a PET/CT scanner

Table 1

Demographics of patients suffering from lymphoma with histopathological and tumor stage information.

Demographics	Values
Age in years (mean \pm SD)	34 ± 11.4
Sex (Female/Male)	4/17
Histopathological findings	No. of patients
Hodgkin lymphoma	13
Diffuse large B-cell lymphoma	5
Follicular lymphoma	3
Ann Arbor stage	No. of patients
Stage I	2
Stage II	2
Stage III	8
Stage IV	9

(Biograph mCT; Siemens Healthcare, Erlangen, Germany). The criteria for patients to undergo a PET scan were fasting for a minimum of 4 h before the examination, and blood glucose levels should be less than 140 mg/dL. Dosage of 6–7 MBq/kg (0.16–0.18 mCi/kg; minimum, 3 mCi) FDG was intravenously injected. After the 45–60-min uptake period, the patients underwent FDG-PET/CT scan. A scout from vertex to mid-thigh was taken, and CT was acquired. There was no contrast injection for the CT imaging. The CT acquisition mode was in spiral method with a reconstruction section thickness of 4 mm and a pitch of 1. After CT, three-dimensional PET data was acquired for 2–3 min per bed position.

2.3. Image analysis

2.3.1. Multimodal 3D-registration between PET and IVIM-DKI volume

The malignant lymph node was localized using 3D-multimodality registration of the PET volume and the IVIM-DKI at $b = 0 \text{ s/mm}^2$ volume. The intensity-based image registration algorithm was implemented using the image registration toolbox ('imregister' function) in MATLAB (under the Statistics Toolbox, The MathWorks, Inc., Natick, MA). One-plus-one evolutionary optimizer configuration was used to perform 3D-multimodality registration [28]. This 3D-multimodality registration was carried out in two stages: STIR was globally registered onto IVIM-DKI at $b = 0 \text{ s/mm}^2$ using affine registration. As shown in Fig. 1, STIR in IVIM-DKI image space was used as a reference volume to bring PET volume in IVIM-DKI image space through rigid registration.

2.3.2. SUV calculation

The standard uptake value (SUV) was calculated using equation (1). SUV_{max} and SUV_{mean} were calculated by taking the maximum and average SUV map of the ROI, respectively, to get the measure of relative FDG uptake. Thus, SUV was calculated as shown below:

$$\text{SUV} = \frac{\text{Mean ROI activity (counts/pixel/sec)} \times \text{calibration factor}}{\text{Injected FDG dose (mCi)} / \text{Body weight (kg)}} \quad (1)$$

where, calibration factor = (mCi/ml)/(counts/pixel/sec).

2.3.3. Quantitative analysis of DWI

The trust region-based algorithm for non-linear least squares optimization was implemented in MATLAB (version 9.1, The MathWorks, Inc., Natick, MA, USA) to estimate ADC and IVIM-DKI parameters. All DWI signals were normalized by DWI signal at $b = 0 \text{ s/mm}^2$. The ADC of each ROI was estimated voxelwise using a monoexponential model using the three different b -values ($0, 500, 1500 \text{ s/mm}^2$) through the following equation (2):

$$\frac{SI}{SI_0} = e^{-b \text{ ADC}} \quad (2)$$

where, SI and SI_0 are diffusion signals with and without a diffusion gradient b in s/mm^2 .

The IVIM-DKI model for multi- b -values was used as in equation (3):

$$\frac{SI}{SI_0} = fe^{-bD^*} + (1-f)e^{-bD+\frac{1}{6}b^2D^2k} \quad (3)$$

The IVIM-DKI was analyzed using two models: (1) standard model as shown in equation (3); and (2) IDTV model, which is an IVIM-DKI model with the TV penalty function method, which minimizes the total variation of a whole 3D-parametric map (equations (4) and (5)) [12,29]. IDTV model utilizes iterations in the optimization procedure involving TV penalty function iteratively [14]. TV minimization as shown in equation (4):

$$\min_H f(H) = \min_H \|H - G\|^2 + \alpha TV(H) \quad (4)$$

where, H and G are expected and observed images (of size $M \times N \times S$), respectively, α is a weight parameter between the data fitting and penalty function, and $TV(H)$ penalty of the 3D parameter map is the L1 norm of discrete image gradient as shown in equation (5):

$$TV(X) = \sum_{i,j,k=1}^{M,N,S} \sqrt{(R_x H)^2 + (R_y H)^2 + (R_z H)^2} \quad (5)$$

where, H is the parameter value at voxel $(i:1,2,3 \dots M; j:1,2,3 \dots N; k:1,2,3 \dots S)$ and $R_x H = H_{(i,j,k)} - H_{(i+1,j,k)}$, $R_y H = H_{(i,j,k)} - H_{(i,j+1,k)}$, and $R_z H = H_{(i,j,k)} - H_{(i,j,k+1)}$. Both the standard and IDTV models were initialized with $D = 1.2 \times 10^{-3} \text{ mm}^2/\text{s}$, $D^* = 13 \times 10^{-3} \text{ mm}^2/\text{s}$, $f = 0.3$, and $k = 0.7$ with bounds for each parameter, $D = [0 \text{ } 0.05] \text{ mm}^2/\text{s}$, $D^* = [0 \text{ } 0.5] \text{ mm}^2/\text{s}$, $f = [0 \text{ } 1]$, and $k = [0 \text{ } 3]$ based on past literatures [10,22].

2.3.4. Localization of ROI

Whole volume ROI for benign and malignant lymph nodes was manually drawn using the MRIcron software [29]. The MR and FDG-PET/CT images was reviewed by one radiologist (D.K.) with more than 10 years of experience in oncological imaging and was informed of the clinical diagnosis and was blinded to the PET/CT findings. 3D-Maximum intensity profile (3D-MIP) of FDG-PET and CT was used to observe overall FDG uptake and locate primary malignant sites in the whole body using Radiant DICOM viewer (version 2021.2, Medixant, Poznan- Poland) as shown in Fig. 2. Fig. 3(a–l) shows the ROI for malignant lymph nodes in HL and NHL if the tumor region was showing avid uptake FDG-PET (hyperintense region) and hyperintense region in IVIM-DKI at b -values = 2000 s/mm^2 . The benign lymph node ROI was drawn on the IVIM-DKI dataset at b -values = 0 s/mm^2 where small lymph nodes in IVIM-DKI at b -values = 0 s/mm^2 showed hyperintensity, and the corresponding region in the SUV map showed no FDG uptake. The focus of this study was to choose one largest tumor burden for malignant lymph nodes in the patient with HL and NHL with total 21 malignant lesions were identified. Total of 21 smallest lymph nodes were delineated by the radiologist for benign lymph nodes. The number of voxels in the ROI of malignant lymph nodes in NHL and HL was 5103.5 ± 4567.48 and 2831.23 ± 3037.08 , respectively, whereas the number of voxels in the benign lymph node ROI was 151.95 ± 81.8 .

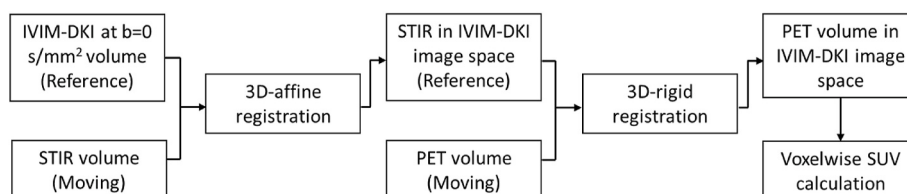


Fig. 1. Schematics of multimodality registration between IVIM-DKI and PET images achieved in two steps: (1) 3D-affine registration between IVIM-DKI volume at $b = 0 \text{ s/mm}^2$ and STIR volume; (2) For improved tumor localization, registered STIR volume was used as reference for registration with PET volume using 3D-rigid registration.

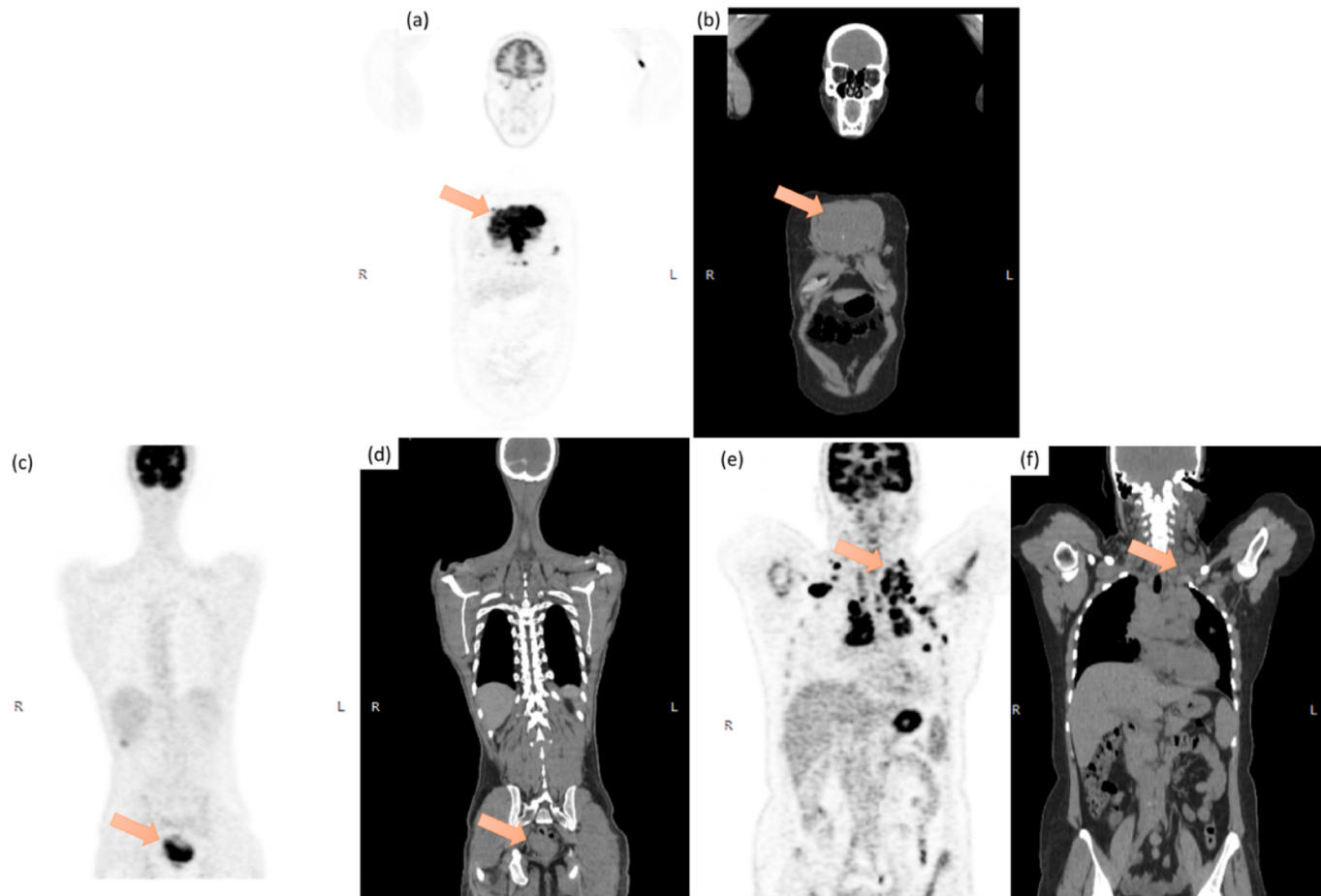


Fig. 2. A representative images showing maximum-intensity profile (MIP) of PET images and CT images used for primary tumor localization in lymphoma. (a–b) MIP and CT image of a 31 year old male patient with Diffuse large B-cell lymphoma (DLBCL) at stage IV and primary tumor being in anterior chest wall (orange arrow). (c–d) MIP and CT image of a 26 year old male patient with follicular lymphoma at stage IV and primary tumor being in rectosigmoid bowel loop (orange arrow). (e–f) MIP and CT image of a 28 year old female patient with Classical Hodgkin lymphoma, Nodular Sclerosis type at stage IV and primary tumor being in left cervical node (orange arrow). (For interpretation of the references to color in this figure legend, the reader is referred to the Web version of this article.)

2.4. Machine learning-based histogram analysis of IVIM-DKI parametric maps

For each ROI, histogram features of the ADC, D, D*, f, and k parametric maps were calculated using histogram with 100 bins. The variance, skewness, kurtosis, energy, and entropy were obtained from the intensity of the histogram in benign and malignant lymph node ROI as shown in Fig. 4. Classification of lesions in lymphoma was performed using linear classifier regularized by logistic regression model to minimize the objective function. This classification model can also be used with small numbers of predictor. Histogram analysis with linear classification model was executed using MATLAB (version 9.9, The MathWorks, Inc., Natick, MA, USA).

2.5. Statistical analysis

All the statistical analysis was performed using MATLAB (version 9.9, The MathWorks, Inc., Natick, MA, USA). The precision of model estimation of the standard and the IDTV models was measured using the coefficient of variation (CV%: standard deviation of ROI $\times 100/\text{mean of ROI}$). If the CV is low, it means the model estimates parameter values precisely. A two-sample Kolmogorov-Smirnov test was used to calculate any significant differences between the IVIM-DKI parameters of benign and malignant lymph nodes in lymphoma. This test was also used to evaluate significant differences between malignant lymph nodes in HL and NHL. To differentiate between benign and malignant lymph nodes

in lymphoma, the diagnostic performance of the IVIM-DKI parameters threshold, accuracy, sensitivity, specificity, F1 score, and area under curve (AUC) were measured using receiver operating characteristics (ROC) analysis. Similarly, using ROC analysis to evaluate the differential diagnosis of IVIM-DKI parameters in lymphoma subtypes (HL and NHL). The linear classifier model was performed using 5-fold cross-validation, where trained sample consisted of 34 and test samples of 8. Performance metric such as accuracy, sensitivity, specificity, F1 score, AUC, and classification error was computed by taking the mean of each cross-validated results.

3. Results

3.1. Qualitative assessment of malignant lymph nodes in lymphoma using IVIM-DKI and PET imaging

Fig. 3 shows that all the malignant lymph nodes had high FDG uptake in the SUV map (figures (b, f, j)) and that the corresponding region can be visualized in IVIM-DKI at $b = 2000\text{s/mm}^2$ (Fig. 3(a, e, i)) and the ADC map (Fig. 3(c, g, k)). Fig. 5 shows a representative image of a 32 year old male patient with DLBCL, stage IV, with a tumor in the anterior chest wall. In the tumor region, a high b-value map, and STIR image showed a hyperintense region, as shown in Fig. 5 (a,c). Also observed in the SUV map with high FDG uptake in the tumor region. As shown in Fig. 3, ADC, D, and f maps showed a hypointense region, and D* and k appeared to be heterogeneously hypointense in the tumor region. Additionally,

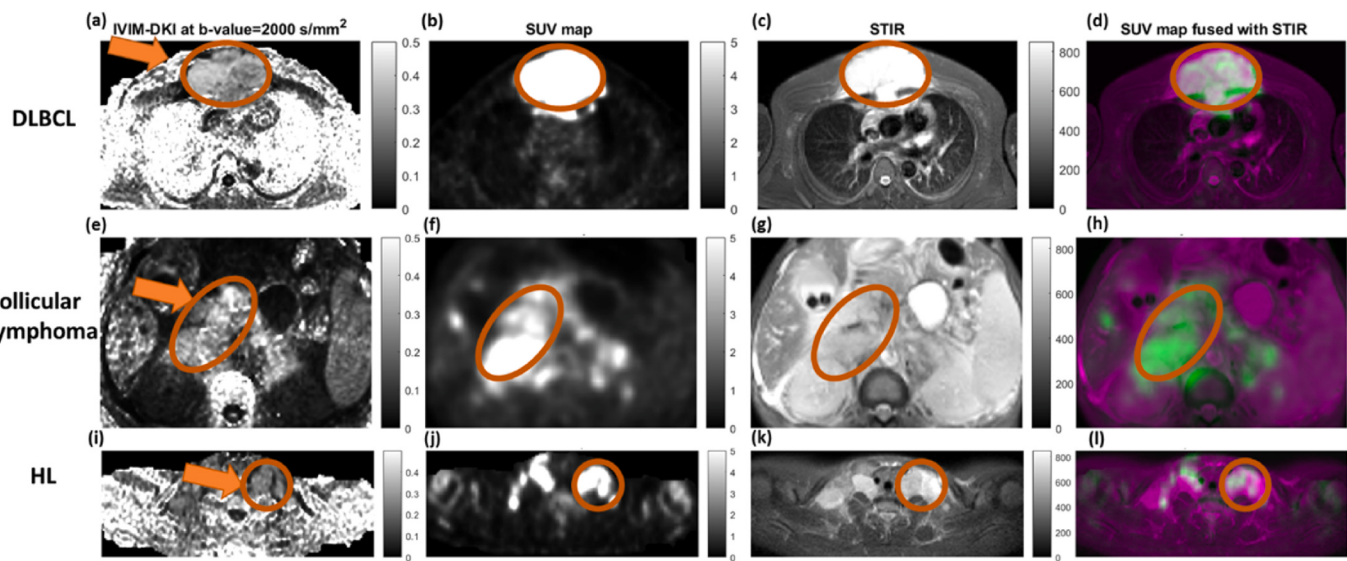


Fig. 3. Representative images of (a–d) of 32 year old male patient suffering from Diffuse large B-cell lymphoma (DLBCL) at stage IV, (e–h) 45 year old male patient suffering from follicular lymphoma at stage III, and (i–l) 28 year old female patient suffering from classical Hodgkin lymphoma (HL), Nodular Sclerosis type at stage IV, showing hyperintensity in tumor region (encircled in white color) in (a,e,i) IVIM-DKI at 2000 s/mm^2 , (b,f,j) SUV map, (c,g,k) STIR image, and (d,h,l) images showing fusion between SUV and STIR image. (For interpretation of the references to color in this figure legend, the reader is referred to the Web version of this article.)

representative images of patients with follicular lymphoma and HL are also presented in the [Supplementary Material Figs. S2–7](#). Qualitatively, IVIM-DKI parametric maps estimated using the IDTV model showed improvement in the quality of parametric maps compared to the standard model.

3.2. Quantitative characterization of benign and malignant lymph nodes in lymphoma using IVIM-DKI and ROC analysis

ADC and IVIM-DKI parameters estimated using the IDTV model were utilized to characterize benign and malignant lymph nodes. [Fig. 6\(a, d, e\)](#) shows that ADC, f, and k values were significantly ($p < 0.05$) lower in malignant lymph nodes than in benign lymph nodes in lymphoma. D and D^* did not show significant differences in the benign and malignant lymph nodes. Mean comparisons between the ADC and IVIM-DKI parameters in benign and malignant lymph nodes in lymphoma is presented in [Table 2](#) showing ADC and IVIM-DKI parameters (f and k) showed significantly ($p < 0.05$) lower values in malignant lymph nodes than in benign lymph nodes. The precision of model estimation was evaluated by calculating CV, where the IDTV model produced significantly ($p < 0.001$) lower CV than the standard model by 42–59% in both benign and malignant lymph nodes for all IVIM-DKI parameters, as shown in [Supplementary Material Table S1](#). This shows that the IDTV model consistently accurately estimates parameter values in any lesion.

ROC analysis was used to measure the diagnostic performance of ADC and IVIM-DKI parameters to characterize benign and malignant lymph nodes in lymphoma. High diagnostic performance was obtained for the f parameter, which showed the highest AUC, accuracy, and F1 score of 0.88, 86%, and 86%, with a cut-off value of 0.223 to differentiate between nodes, as shown in [Table 3](#). Even the k parameter showed high diagnostic performance, with AUC, accuracy, and F1 score of 0.83, 81%, and 79%, with a cut-off value of 0.993. Furthermore, ADC showed moderate performance with AUC, accuracy, and F1 score of 0.71, 71%, and 73% with a cut-off value of $1.078 \times 10^{-3} \text{ s/mm}^2$.

3.3. Histogram analysis in characterization of benign and malignant lymph nodes in lymphoma using IVIM-DKI parametric maps

[Table 4](#) depicts the classification performance of the IVIM-DKI

parametric maps' histogram features using a linear classifier. For each parameter, various combinations of histogram features were employed for classification. Overall combination of five features, variance, skewness, kurtosis, entropy, and energy yielded the highest accuracy (84.8–94.8%) and AUC (0.82–0.97). It was also observed that performance of linear classifier model improved with increasing number of histogram features of ADC and k. However, linear classifier model with only one histogram feature of D can perform classification with high accuracy for variance with 81.8%, skewness with 74.6%, kurtosis with 89.4%, entropy with 87.4%, except for entropy (58.2%). For D^* , combination of variance and skewness features showed high accuracy of 94.8% and AUC of 1. Whereas for f, combination of variance, skewness and kurtosis showed highest accuracy amongst all combination of histogram features of the parametric maps with accuracy of 97.2% and AUC of 1.

3.4. Quantitative characterization of malignant lymphoma subtypes using IVIM-DKI, PET imaging and ROC analysis

HL and NHL were also characterized using IVIM-DKI parameters estimated using the IDTV model and PET parameters. [Fig. 7\(a–d\)](#) shows that ADC, D, D^* , and f were significantly ($p < 0.05$) higher in HL than in NHL. k, SUVmean, and SUVmax, on the other hand, did not differ significantly between HL and NHL. The mean of ADC, IVIM-DKI, and PET parameters were compared between malignant lymph nodes in HL and NHL. This is presented in [Table 5](#) showing only ADC and IVIM-DKI parameters (D, D^* , and f) showed significant differences.

ROC analysis was used to evaluate the differential diagnosis of NHL against HL using ADC, IVIM-DKI, and PET parameters. D^* showed the highest AUC of 0.85 with accuracy and an F1 score of 80% and 82%, respectively, with a cut-off value of $23.458 \times 10^{-3} \text{ s/mm}^2$. Additionally, ADC and D showed high AUC, accuracy, and F1 score of 0.84, 85%, 88%, respectively, and the cut-off values of $0.828 \times 10^{-3} \text{ s/mm}^2$ and $0.772 \times 10^{-3} \text{ s/mm}^2$, respectively, as shown in [Table 6](#) f showed moderate AUC, accuracy and F1 score of 0.74, 75%, and 78%, respectively with a cut-off value of 0.193. PET parameters such as SUV_{mean} and SUV_{max} performed poorly in differentiating NHL from HL with AUC, accuracy, and F1 score of >0.58, 70%, and 77%.

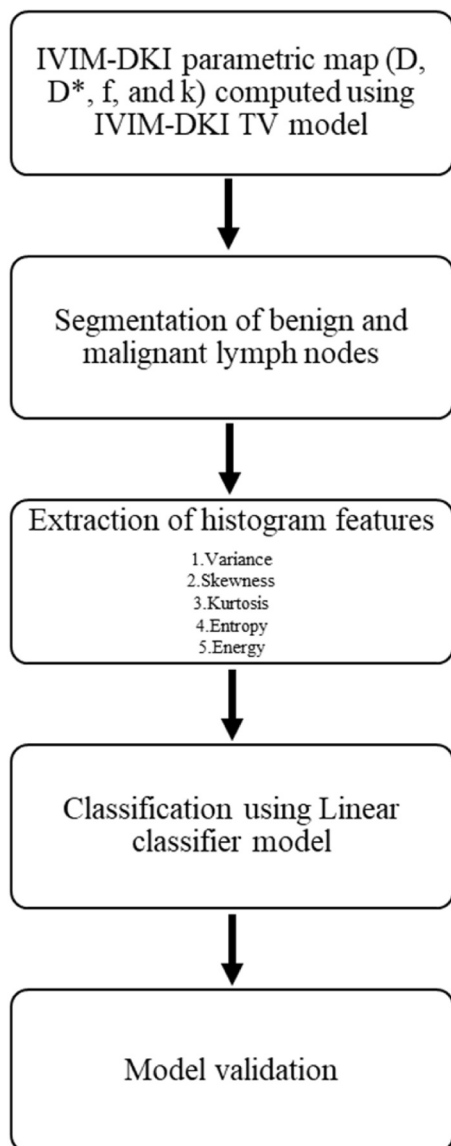


Fig. 4. Schematics showing machine learning-based classification using linear classifier model and histogram features of ADC and IVIM-DKI parameters.

3.5. Correlation between ADC and IVIM-DKI parameters with PET parameters in lymphoma

There was a positive correlation between ADC ($\rho = 0.5$, $p < 0.05$), D ($\rho = 0.48$, $p < 0.05$), D^* ($\rho = 0.49$, $p < 0.05$) with SUV_{mean} as shown in Fig. 8(a-c). There was no correlation observed between f or k with SUV_{mean} . SUV_{max} and SUV_{mean} showed a significant correlation with rho of 0.85 ($p < 0.001$), as shown in Fig. 8(h).

4. Discussion

Quantitative DWI technique, such as IVIM-DKI offer quantitative metrics that evaluate physiological processes in the tissue at microscopic level. This method provides cost-effective, non-invasive, and radiation-free cancer management and lymph node characterization. However, IVIM-DKI has a substantial parameter estimation error owing to the assumption that nearby voxels are independent entities for model-based analysis. In this study, the IVIM-DKI model with the TV method was used to account for this assumption and to generate high-precision, high-quality parametric maps for enhanced clinical interpretation. f and k were computed using the IDTV model and ADC quantitatively characterized benign and malignant lymph nodes, with benign lymph nodes demonstrating significantly higher ADC, f, and k than malignant lymph nodes. Malignant lymph nodes were further classified as lymphoma subtypes, including HL and NHL. D, D^* , and f estimated by the IDTV model and ADC were significantly higher in the NHL compared to the HL. A similar trend was seen for the differential diagnosis of benign and malignant lymph nodes using f, k, and ADC, demonstrating high AUC and accuracy. D, D^* , f, and ADC demonstrated a high AUC and accuracy in differentiating malignant lymph nodes in NHL and HL. Additionally, the correlation between ADC, IVIM-DKI, and PET parameters was investigated, and ADC, D, and D^* correlated positively with SUV_{mean} . This study indicates that IVIM-DKI with parametric reconstruction can quantitatively provide improved lymph node characterization with higher diagnostic performance than FDG-PET/CT.

DWI has shown potential in the characterization of benign and malignant lesions in many pathologies, such as head and neck, prostate, and renal tissue [30–33]. In the present study, we characterized benign and malignant lymph nodes in lymphoma using ADC and IVIM-DKI parameters. In benign lymph nodes, ADC was higher than in malignant lymph nodes. This is possibly due to benign lymph nodes being rich in lymphocytes and plasma cells with low cell density, whereas malignant nodes have a high nucleus-to-cytoplasm ratio and cell density with low extracellular space [34]. ADC is measured using a conventional monoexponential function and has shown its potential in the differentiation of benign and malignant lymph nodes [8,24,30,35]. However,

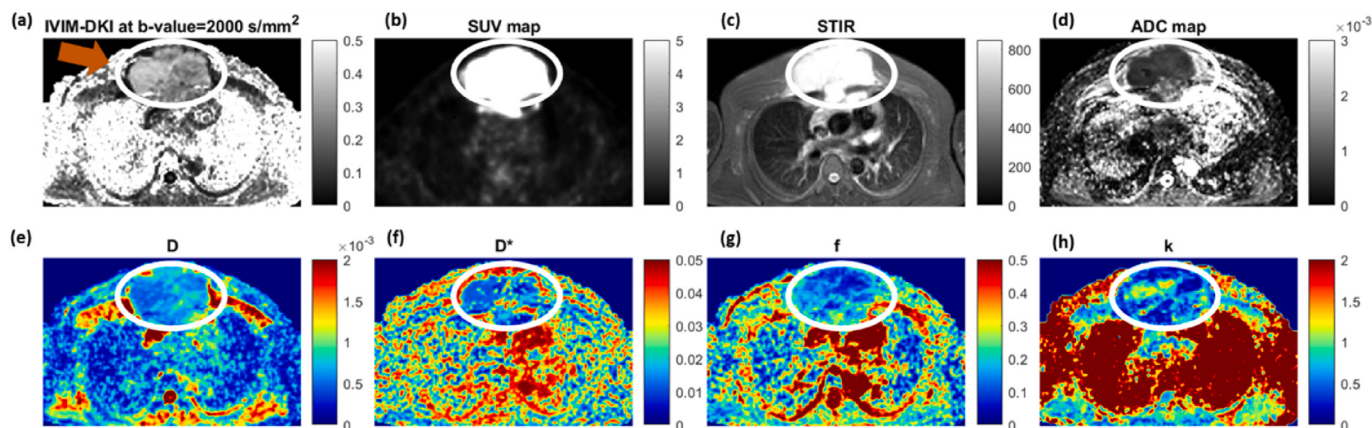


Fig. 5. Representative images of 32 year old male patient suffering from Diffuse large B-cell lymphoma (DLBCL) at stage IV showing (a) IVIM-DKI at 2000 s/mm^2 , (b) SUV map, (c) STIR images, and (d) ADC map. (e) D, (f, j) D^* , (g, k) f, and (h, l) k maps. In tumor region (white encircled), hyperintensity was observed on (a) IVIM-DKI at 2000 s/mm^2 , (b) SUV map, (c) STIR images, (f) D^* map, and (h) k map and hypointensity was observed on (d) ADC map, (e) D map, and (g) f map.

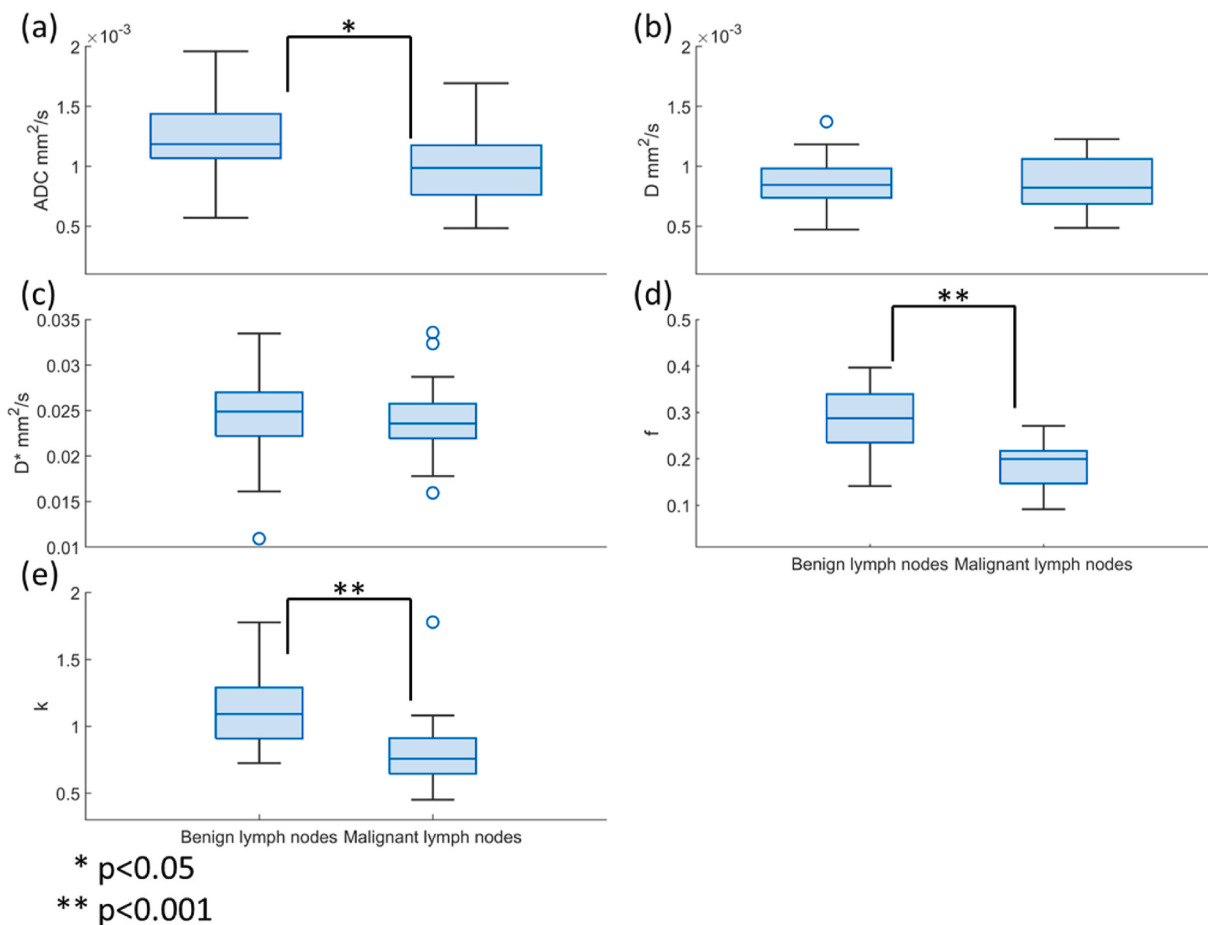


Fig. 6. Boxplot showing comparison between ADC and IVIM-DKI parameters quantified from IDTV model in benign and malignant lymph nodes. ADC, f, and k were significantly ($p < 0.05$) lower in malignant lymph node than benign lymph node.

Table 2

Quantitative comparison between mean of ADC and IVIM-DKI parameters in benign and malignant lymph node. ADC and f and k estimated using IDTV model showed significantly ($p < 0.05$) lower in malignant lymph nodes than in benign lymph nodes.

DWI/IVIM-DKI parameters	Benign lymph node	Malignant lymph node	P-value
ADC ^a	1.25 ± 0.33	0.997 ± 0.31	<0.05
D ^a	0.86 ± 0.21	0.86 ± 0.22	N.S.
D* ^a	24.27 ± 5.2	23.99 ± 4.35	N.S.
f	0.28 ± 0.07	0.19 ± 0.05	<0.001
k	1.13 ± 0.27	0.79 ± 0.29	<0.001

All values are in mean \pm SD.

^a ADC, D, and D* are expressed in $10^{-3} \text{ mm}^2/\text{s}$; ADC: Apparent diffusion coefficient; D: Diffusion coefficient; DWI: Diffusion-weighted imaging; D*: Pseudo-diffusion coefficient; f: Perfusion fraction; k: Kurtosis; IVIM-DKI: Intravoxel Incoherent motion-diffusion kurtosis imaging; N.S.: Non-significant.

IVIM-DKI can produce quantitative diffusion and perfusion information with additional kurtosis information on tumor heterogeneity at low b-values (100 s/mm^2) and high b-values ($>1500 \text{ s/mm}^2$), respectively [10,11,36]. In this study, a parametric reconstruction method such as TV was employed with the IVIM-DKI model, which has been shown to remove any spurious values while estimating parameters and improve the characterization of prostatic lesions [12]. The results showed that f and k estimated using the IDTV model were also able to differentiate benign and malignant lymph nodes. Similar results were also seen in previous studies [31,37]. f represents blood volume fraction, and higher perfusion in benign nodes may indicate the presence of increased blood flow and high permeability [4]. However, k was lower in malignant than in benign lymph nodes. This was also seen in previous studies where k was higher in benign lesions than in soft tissue masses due to the presence of inflammation or fibrous tissues [38]. D and D* didn't show any significant differences between benign and malignant nodes. While f and k showed higher AUC and accuracy compared to ADC in differentiation between benign and malignant lymph nodes. Also, the AUC of f and k in

Table 3

Characterizing of ADC and IVIM-DKI parameters estimated using IDTV model in benign and malignant lymph nodes in the lymphoma using ROC analysis.

DWI parameters	Threshold	Accuracy %	Sensitivity %	Specificity %	F1 score %	AUC (CI)	p-value
ADC ^a	0.001077537	71	76	67	73	0.71 (0.56–0.90)	0.004
D ^a	0.000828249	60	62	57	60	0.53 (0.35–0.7)	0.3675
D* ^a	0.02436449	64	62	67	63	0.58 (0.41–0.80)	0.1749
f	0.222852889	86	90	81	86	0.88 (0.77–1)	<0.001
k	0.992826158	81	71	90	79	0.83 (0.7–1)	<0.001

^a ADC, D, and D* are expressed in mm^2/s ; ADC: Apparent diffusion coefficient; AUC: Area under curve; CI: Confidence interval; D: Diffusion coefficient; DWI: Diffusion-weighted imaging; D*: Pseudo-diffusion coefficient; f: Perfusion fraction; k: Kurtosis; IVIM-DKI: Intravoxel Incoherent motion-diffusion kurtosis imaging.

Table 4

Performance of histogram features extracted from the ADC and IVIM-DKI parameters in classification of benign and malignant lymph nodes in the lymphoma.

Histogram features	Accuracy	Sensitivity	Specificity	F1 score	AUC	Classification Error
Variance						
ADC	79.6 ± 10.6	77.4 ± 8.8	83.6 ± 12	77.6 ± 10.0	0.82 ± 0.17	20.6 ± 9.1
D	81.8 ± 12.0	79.4 ± 14.4	88.4 ± 7.1	78.4 ± 14.8	0.81 ± 0.15	18.6 ± 13.0
D*	76.0 ± 14.1	71.8 ± 18.2	85.3 ± 10.5	68.6 ± 22.3	0.73 ± 0.26	26.0 ± 16.4
f	74.0 ± 15.2	71.6 ± 13.8	87.0 ± 4.7	68.0 ± 21.2	0.70 ± 0.28	25.4 ± 12.6
k	79.0 ± 14.4	76.0 ± 15.5	87.6 ± 8.0	74.4 ± 17.5	0.86 ± 0.13	21.8 ± 14.2
Skewness						
ADC	64.8 ± 20.6	64.2 ± 19.2	68.8 ± 30.0	58.6 ± 26.5	0.80 ± 0.22	35.2 ± 20.3
D	74.6 ± 11.5	73.2 ± 13.1	76.4 ± 14.8	72.2 ± 13.2	0.81 ± 0.11	26.2 ± 13.0
D*	52.6 ± 14.4	52.4 ± 15.5	46.4 ± 22.9	47.8 ± 19.9	0.56 ± 0.12	46.8 ± 14.0
f	79.0 ± 7.5	77.2 ± 8.3	82.2 ± 8.0	76.8 ± 8.8	0.89 ± 0.11	21.4 ± 8.0
k	89.6 ± 5.9	88.4 ± 6.9	92.0 ± 4.5	88.4 ± 6.7	0.98 ± 0.02	10.4 ± 6.1
Kurtosis						
ADC	85.0 ± 13.5	85.4 ± 13.6	86.2 ± 13.8	84.4 ± 13.8	0.92 ± 0.12	15.2 ± 13.5
D	89.4 ± 11.9	89.0 ± 13.5	92.2 ± 7.6	87.8 ± 14.3	0.97 ± 0.06	10.4 ± 12.3
D*	65.2 ± 21.1	62.4 ± 22.4	65.8 ± 24.5	59.2 ± 25.1	0.63 ± 0.29	35.8 ± 21.5
f	73.6 ± 9.2	71.6 ± 11.3	75.4 ± 12.2	70.8 ± 11.5	0.77 ± 0.27	27.2 ± 10.8
k	57.8 ± 10.2	53.0 ± 13.0	54.0 ± 27.2	45.0 ± 16.5	0.58 ± 0.22	43.0 ± 12.6
Energy						
ADC	76.6 ± 17.7	76 ± 18.5	76.6 ± 18.6	75.4 ± 18.8	0.87 ± 0.13	23.4 ± 18.1
D	87.4 ± 15.1	87.8 ± 15.1	88.2 ± 15.1	87.0 ± 15.5	0.95 ± 0.11	12.8 ± 16
D*	89.6 ± 5.9	88.4 ± 6.9	92.0 ± 4.7	88.4 ± 6.6	0.90 ± 0.14	11 ± 6.4
f	58.2 ± 9.0	53.4 ± 7.6	83.0 ± 0.01	41.0 ± 13.6	0.45 ± 0.14	42 ± 6.7
k	79.6 ± 10.6	75.8 ± 15.2	88.3 ± 3.5	73.2 ± 20.4	0.75 ± 0.14	22.8 ± 14
Entropy						
ADC	76.2 ± 21.3	75.8 ± 19.5	79 ± 21.2	75.0 ± 21.3	0.77 ± 0.20	23.6 ± 20.5
D	58.2 ± 9.0	53.4 ± 7.6	83.0 ± 0.01	41.0 ± 13.6	0.44 ± 0.24	42 ± 6.7
D*	86.8 ± 13.6	86.6 ± 12.7	91.0 ± 9.3	85.8 ± 14.0	0.88 ± 0.17	13 ± 12.7
f	58.0 ± 5.4	52.6 ± 5.8	79.0 ± 0.01	39.8 ± 9.2	0.55 ± 0.20	42.8 ± 4.9
k	79.0 ± 14.4	77.6 ± 14.7	87.0 ± 8.3	75.6 ± 17.1	0.79 ± 0.14	20.2 ± 13.5
Variance + Skewness						
ADC	79.4 ± 19.1	78.6 ± 19.6	85.0 ± 15.6	76.6 ± 21.6	0.86 ± 0.21	20 ± 18.4
D	73.6 ± 20.1	72 ± 21.6	74.8 ± 28.3	68.8 ± 25.3	0.93 ± 0.11	27.2 ± 19.7
D*	94.8 ± 7.2	94.2 ± 8.1	96.0 ± 5.5	94.2 ± 8.0	1.0 ± 0.001	5.2 ± 7.3
f	92.4 ± 7.0	91.8 ± 7.8	94.0 ± 5.5	91.6 ± 7.8	0.95 ± 0.07	8.0 ± 7.4
k	79.2 ± 11.5	76.8 ± 11.1	86.8 ± 5.5	75.4 ± 14.0	0.76 ± 0.21	21.6 ± 9.6
Variance + Skewness + Kurtosis						
ADC	89.6 ± 5.9	88.4 ± 6.9	92.0 ± 4.7	88.4 ± 6.6	0.95 ± 0.07	11.6 ± 6.5
D	71.2 ± 17.1	69.2 ± 16.1	81.0 ± 15.4	65.6 ± 22.0	0.90 ± 0.1	28.8 ± 15.6
D*	84.6 ± 13.4	84.8 ± 13.7	89.0 ± 7.5	82.6 ± 16.1	0.81 ± 0.15	14.8 ± 12.3
f	97.2 ± 6.3	97.6 ± 5.4	97.6 ± 5.4	97.2 ± 6.3	1 ± 0.001	2.8 ± 6.3
k	76.8 ± 13.9	74.4 ± 15.0	86.2 ± 8.1	72.2 ± 16.7	0.75 ± 0.27	23.2 ± 13.7
Variance + Skewness + Kurtosis + Energy						
ADC	90.0 ± 5.7	90.8 ± 5.2	91.2 ± 5	89.4 ± 5.9	0.98 ± 0.04	9.4 ± 5.4
D	94.8 ± 7.2	94.6 ± 7.8	95.6 ± 6.1	94.2 ± 8.0	0.98 ± 0.04	5.2 ± 7.3
D*	84.8 ± 16.1	84.2 ± 16.1	90.4 ± 9.6	82.6 ± 18.8	0.82 ± 0.22	14.2 ± 14.6
f	92.6 ± 11.1	92.2 ± 11.9	92.6 ± 11.8	92.0 ± 12.0	0.97 ± 0.04	7.4 ± 11.4
k	71.4 ± 14.5	68.4 ± 14.3	85.0 ± 7.0	63.4 ± 20.9	0.78 ± 0.06	28.6 ± 13.2
Variance + Skewness + Kurtosis + Energy + Entropy						
ADC	92.4 ± 7.0	93.2 ± 6.3	93.2 ± 6.3	92.0 ± 7.3	0.95 ± 0.07	7.2 ± 6.7
D	94.8 ± 7.2	95.2 ± 6.6	95.6 ± 6.1	94.6 ± 7.4	0.95 ± 0.11	5.0 ± 6.9
D*	84.8 ± 16.1	84.2 ± 16.1	90.4 ± 9.6	82.6 ± 18.8	0.82 ± 0.2	14.2 ± 14.6
f	92.6 ± 11.1	92.2 ± 11.9	92.6 ± 11.8	92.0 ± 12.0	0.97 ± 0.04	7.4 ± 11.4
k	89.6 ± 5.9	87.4 ± 7.4	92.4 ± 4.3	88.0 ± 6.8	0.84 ± 0.12	11.2 ± 6.5

ADC: Apparent diffusion coefficient; AUC: Area under curve; D: Diffusion coefficient; D*: Pseudo-diffusion coefficient; f: Perfusion fraction; k: Kurtosis.

the differentiation of benign and malignant lymph nodes reported by previous studies was lower than in our study [31,39]. This demonstrates that the IDTV model may provide high diagnostic performance even when parameters are employed individually.

In this study, we compared the effectiveness of using a histogram analysis of ADC vs IVIM-DKI parametric maps for identifying lymph nodes as benign or malignant in patients with lymphoma. A linear classifier model was provided with different combinations of histogram features. Linear classifier models using logistic regression is successfully used in the classification of benign and malignant lesions in different cancers [40–42]. A recent study found that IVIM-DKI combined with the TV approach can enhance the classification of pancreatic lesions utilizing texture analysis and an artificial neural network [18]. However, no research has utilized histogram analysis of IVIM-DKI parametric maps with machine learning-based classification of lymphoma lesions. In this

investigation, D parameter with any combination of characteristics achieved good accuracy, even with just one histogram feature. High diagnostic performance with ADC and k required the use of at least four histogram features combinations. However, D* and f demonstrated that even with two or three histogram features, they can be used to detect lesion with high diagnostic performance.

Characterization of malignant lymph nodes in lymphoma subtypes can help to optimize the prognosis and treatment approaches. Using ADC, IVIM-DKI, and PET parameters, the characterization of NHL and HL was investigated in this study. ADC was lower in NHL lymph nodes than in HL, and similar results were obtained in previous literature [2, 43]. The low cellularity in the DLBCL might be contributing to the low ADC value in NHL. There are limited studies on IVIM and IVIM-DKI analysis on the characterization of lymphoma subtypes. Thus, in this study, IVIM-DKI parameters such as D, D*, and f showed lower values in

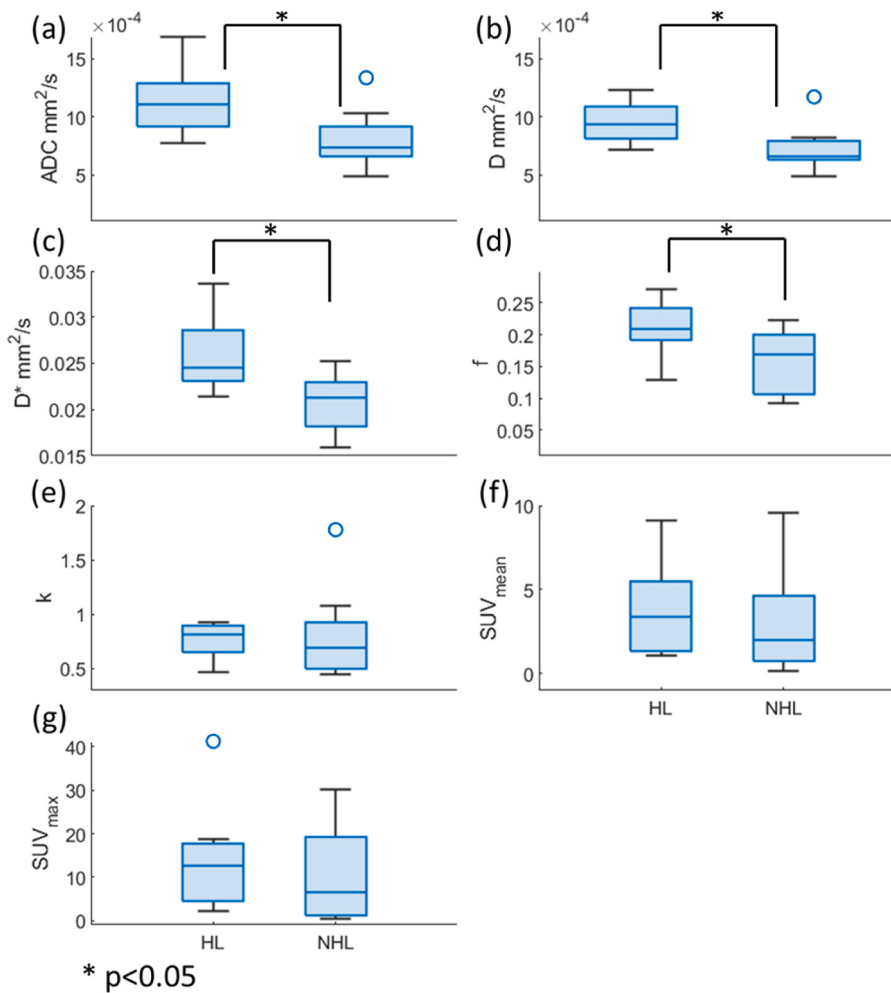


Fig. 7. Boxplot showing comparison between ADC and SUV parameters and IVIM-DKI parameters quantified from IDTV model in Hodgkin lymphoma (HL) and non-Hodgkin lymphoma (NHL). ADC, D, D^* , and f were significantly ($p < 0.05$) lower in NHL than HL.

Table 5

Quantitative comparison between mean of ADC, IVIM-DKI, and SUV parameters in NHL and HL. ADC and D, D^* , and f estimated using IDTV model showed significantly ($p < 0.05$) lower in malignant lymph nodes of NHL than in HL.

DWI/IVIM-DKI parameters	NHL	HL	P-value
ADC ^a	0.81 ± 0.27	1.14 ± 0.28	<0.05
D ^a	0.73 ± 0.2	0.96 ± 0.18	<0.05
D^* ^a	20.75 ± 3.11	26.11 ± 3.97	<0.05
f	0.16 ± 0.05	0.21 ± 0.04	<0.05
k	0.81 ± 0.44	0.77 ± 0.15	N.S.
SUV _{mean}	3.06 ± 3.22	3.73 ± 2.61	N.S.
SUV _{max}	10.56 ± 11.19	13.3 ± 10.8	N.S.

All values are in mean \pm SD.

^a ADC, D, and D^* are expressed in $10^{-3} \text{ mm}^2/\text{s}$; ADC: Apparent diffusion coefficient; D: Diffusion coefficient; DWI: Diffusion-weighted imaging; D^* : Pseudo-diffusion coefficient; f: Perfusion fraction; k: Kurtosis; HL: Hodgkin lymphoma; IVIM-DKI: Intravoxel Incoherent motion-diffusion kurtosis imaging; NHL: Non-Hodgkin lymphoma; N.S.: Non-significant.

NHL than in HL with high diagnostic performance. NHL-affected lymph nodes are hypoperfused and might have caused low D^* and f [44]. However, PET parameters such as SUV_{max} and SUV_{mean} didn't show significant differences between NHL and HL, with poorer diagnostic performance than ADC or IVIM-DKI parameters.

The correlation between ADC and DWI parameters with SUV was investigated in this study. ADC, D, D^* , and SUV_{max} were positively

correlated with SUV_{mean} in malignant lymph nodes of lymphoma. Recent studies could not establish the correlation between PET and ADC or IVIM parameters [45,46]. Some studies found a negative correlation between ADC and SUV parameters [47,48]. The examining the link between glucose metabolism and cellular density, diffusion, and perfusion have not yet been fully explored, and further studies are needed with larger data sets for conclusive evidence.

The study has some limitations. First, it had a low sample size and was conducted at a single institution, which could have unavoidably introduced selection bias. A large multicentric dataset would be needed for conclusive evidence. Second, further subtyping of NHL was not performed due to low sample size of NHL. Third, since the ROI was drawn manually by a single radiologist, inter-observer variability could not be measured. Fourth, owing to the long scan duration and low image quality due to motion artifacts, whole-body IVIM-DKI was not implemented. As a result, different acquisition parameters were used for the mid-brain area to the abdomen and mid-thigh region. Fifth, ROI for malignant lymph nodes was drawn only on the large site of the tumor. Future studies can investigate small lymph node involvement using IVIM-DKI. Finally, only malignant lymph nodes were histologically verified. However, benign nodes were not biopsy-proven since biopsies of benign-looking lymph nodes are not recommended in our clinical setting. Thus, IVIM-DKI and whole-body PET imaging were only employed to locate benign nodes.

The future scope of this study would be to examine the IVIM-DKI with TV method on large multi-centric data of lymphoma patients.

Table 6

Characterizing of ADC, PET and IVIM-DKI parameters estimated using IDTV model in HL and NHL using ROC analysis.

DWI/PET parameters	Threshold	Accuracy %	Sensitivity %	Specificity %	F1 score %	AUC (CI)	P-value
ADC ^a	0.000827576	85	92	75	88	0.84 (0.64–1)	0.0003
D ^a	0.000771937	85	92	75	88	0.84 (0.64–1)	0.0004
D* ^a	0.023457613	80	75	88	82	0.85 (0.66–1)	0.0002
f	0.192907741	75	75	75	78	0.74 (0.51–0.98)	0.0212
k	0.817871955	60	50	75	60	0.38 (0.13–0.63)	0.8261
SUV _{mean}	1.155686179	70	83	50	77	0.62 (0.36–0.88)	0.1819
SUV _{max}	2.575486179	70	83	50	77	0.58 (0.32–0.85)	0.2688

^a ADC, D, and D* are expressed in mm²/s; ADC: Apparent diffusion coefficient; AUC: Area under curve; CI: Confidence interval; D: Diffusion coefficient; DWI: Diffusion-weighted imaging; D*: Pseudo-diffusion coefficient; f: Perfusion fraction; k: Kurtosis; IVIM-DKI: Intravoxel Incoherent motion-diffusion kurtosis imaging; SUVmax: maximum of Standard uptake value; SUVmean: mean of standard uptake value.

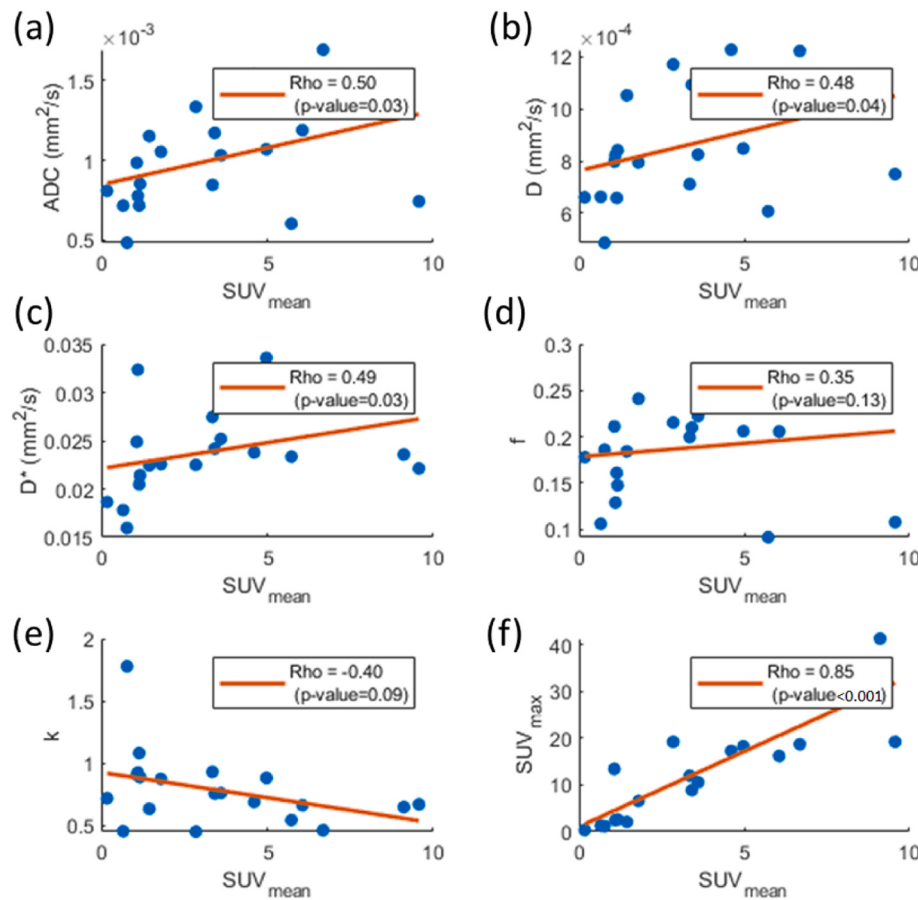


Fig. 8. Correlation plots showing correlation between ADC and IVIM-DKI parameters, SUV_{max} with SUV_{mean} of the patients with lymphoma. ADC, D, D*, and SUV_{max} positively correlated with SUV_{mean}.

Secondly, automated ROI detection can be employed using the histogram or texture features of the lesions using deep learning [49]. Thirdly, histogram analysis can also aid in surgical planning of tumor resection. Lastly, blood circulation changes with tumor growth, thus, 3D flow of cross magnetofluid [50,51] can help to understand 3D flow of blood and thereby providing information on tumor microstructure.

5. Conclusion

In conclusion, our preliminary results showed that IVIM-DKI with the TV method was feasible in the characterization of benign and malignant lymph nodes in lymphoma and further classification of lymphoma subtypes were comparable to FDG-PET/CT. ADC, f, and k showed significant differences between benign and malignant lymph nodes in lymphoma. Whereas ADC, D, D*, and f were significantly different in

malignant lymph nodes of NHL and HL. IVIM-DKI parameters showed higher diagnostic performance than ADC, and PET parameters in the characterization of HL and NHL. The histogram analysis also showed that IVIM-DKI with TV method can improve the lesion detection with any combination of histogram features of D, D*, and f. The correlation was also established between ADC, D, D*, and SUV_{max} with SUV_{mean}. IVIM-DKI has the wide potential for assessment of lymph nodes in lymphoma.

Credit author statement

Archana Vadiraj Malagi: Conceptualization, Methodology, Software, Validation, Formal analysis, Data curation, Writing – original draft, Writing – review & editing, Visualization, Devasenathipathy Kandasamy: Conceptualization, Methodology, Writing – review & editing,

Supervision, Project administration, Deepam Pushpam: Conceptualization, Methodology, Resources. Supervision, Project administration, Kedar Kare: Conceptualization, Methodology, Writing – review & editing, Supervision, Raju Sharma: Writing – review & editing, Visualization, Rakesh Kumar: Resources, Writing – review & editing, Visualization, Sameer Bakshi: Conceptualization, Methodology, Investigation, Resources, Writing – review & editing, Visualization, Amit Mehndiratta: Conceptualization, Methodology, Software, Validation, Writing – review & editing, Supervision, Project administration, Funding acquisition.

Funding sources

The authors would like to thank SERB, Department of Science and Technology, Government of India, India (CRG/2021/005342) for the funding support.

Declaration of competing interest

The authors declare that they have no known competing financial interests or personal relationships that could have appeared to influence the work reported in this paper.

Data availability

Data will be made available on request.

Appendix A. Supplementary data

Supplementary data to this article can be found online at <https://doi.org/10.1016/j.rineng.2023.100928>.

References

- [1] V. Radhakrishnan, et al., Management of hodgkins lymphoma: ICMR consensus document, Indian J. Pediatr. 84 (5) (May 2017) 371–381, <https://doi.org/10.1007/s12098-017-2304-6>.
- [2] F. Mosavi, C. Wassberg, J. Selling, D. Molin, H. Ahlström, Whole-body diffusion-weighted MRI and 18F-FDG PET/CT can discriminate between different lymphoma subtypes, Clin. Radiol. 70 (11) (2015) 1229–1236, <https://doi.org/10.1016/j.crad.2015.06.087>.
- [3] S. Bakhshi, et al., Pediatric nonlymphoblastic non-Hodgkin lymphoma: baseline, interim, and posttreatment PET/CT versus contrast-enhanced CT for evaluation—a prospective study, Radiology 262 (3) (2012) 956–968.
- [4] C. Xu, S. Du, S. Zhang, B. Wang, C. Dong, H. Sun, Value of integrated PET-IVIM MR in assessing metastases in hypermetabolic pelvic lymph nodes in cervical cancer: a multi-parameter study, Eur. Radiol. 30 (5) (May 2020) 2483–2492, <https://doi.org/10.1007/s00330-019-06611-z>.
- [5] P. Sharma, A. Gupta, C. Patel, S. Bakhshi, A. Malhotra, R. Kumar, Pediatric lymphoma: metabolic tumor burden as a quantitative index for treatment response evaluation, Ann. Nucl. Med. 26 (1) (2012) 58–66, <https://doi.org/10.1007/s12149-011-0539-2>. Jan.
- [6] S. Bakhshi, et al., Posttreatment PET/CT rather than interim PET/CT using deauville criteria predicts outcome in pediatric Hodgkin lymphoma: a prospective study comparing PET/CT with conventional imaging, J. Nucl. Med. 58 (4) (2017) 577–583, <https://doi.org/10.2967/jnumed.116.176511>.
- [7] B.D. Cheson, et al., Recommendations for initial evaluation, staging, and response assessment of Hodgkin and non-hodgkin lymphoma: the lugano classification, J. Clin. Oncol. 32 (27) (2014) 3059–3067, Sep, <https://doi.org/10.1200/JCO.2013.54.8800>.
- [8] K.N. De Pepe, et al., Improving lymph node characterization in staging malignant lymphoma using first-order ADC texture analysis from whole-body diffusion-weighted MRI, J. Magn. Reson. Imag. 48 (4) (2018) 897–906, <https://doi.org/10.1002/jmri.26034>.
- [9] D. Albano, C. Patti, D. Matranga, R. Lagalla, M. Midiri, M. Galia, Whole-body diffusion-weighted MR and FDG-PET/CT in Hodgkin Lymphoma: predictive role before treatment and early assessment after two courses of ABVD, Eur. J. Radiol. 103 (April) (2018) 90–98, <https://doi.org/10.1016/j.ejrad.2018.04.014>.
- [10] Y. Lu, J.F.A. Jansen, Y. Mazaheri, H.E. Stambuk, J.A. Koutcher, A. Shukla-Dave, Extension of the intravoxel incoherent motion model to non-Gaussian diffusion in head and neck cancer, J. Magn. Reson. Imag. 36 (5) (2012) 1088–1096, <https://doi.org/10.1002/jmri.23770>.
- [11] J.H. Jensen, J.A. Helpern, A. Ramani, H. Lu, K. Kaczynski, Diffusional kurtosis imaging: the quantification of non-Gaussian water diffusion by means of magnetic resonance imaging, Magn. Reson. Med. 53 (6) (2005) 1432–1440, <https://doi.org/10.1002/mrm.20508>.
- [12] A.V. Malagi, et al., IVIM-DKI for differentiation between prostate cancer and benign prostatic hyperplasia: comparison of 1.5 T vs. 3 T MRI, Magnetic Resonance Materials in Physics, Biology and Medicine (May 2021), <https://doi.org/10.1007/s10334-021-00932-1>.
- [13] A.V. Malagi, et al., Qualitative and quantitative comparison between IVIM-DKI and PET/CT imaging in lymphoma," presented at the, Proceedings of the 29th Annual Meeting of ISMRM (2021) 3665.
- [14] E.B. Kayal, et al., Quantitative analysis of intravoxel incoherent motion (IVIM) diffusion MRI using total variation and huber penalty function, Med. Phys. 44 (11) (2017) 5849–5858, <https://doi.org/10.1002/mp.12520>.
- [15] E.B. Kayal, D. Kandasamy, K. Khare, S. Bakhshi, R. Sharma, A. Mehndiratta, Intravoxel incoherent motion (IVIM) for response assessment in patients with osteosarcoma undergoing neoadjuvant chemotherapy, European journal of radiology 119 (2019), 108635.
- [16] E. Baidya Kayal, et al., Non-invasive intravoxel incoherent motion MRI in prediction of histopathological response to neoadjuvant chemotherapy and survival outcome in osteosarcoma at the time of diagnosis, J. Transl. Med. 20 (1) (2022) 625, <https://doi.org/10.1186/s12967-022-03838-1>. Dec.
- [17] A.V. Malagi, C.J. Das, K. Khare, F. Calamante, A. Mehndiratta, Effect of combination and number of b values in IVIM analysis with post-processing methodology: simulation and clinical study, Magn. Reson. Mater. Phys. 32 (5) (Oct. 2019) 519–527, <https://doi.org/10.1007/s10334-019-00764-0>.
- [18] A.V. Malagi, et al., Pancreatic mass characterization using IVIM-DKI MRI and machine learning-based multi-parametric texture analysis, Bioengineering 10 (1) (Jan. 2023), <https://doi.org/10.3390/bioengineering10010083>. Art. no. 1.
- [19] C. Liu, C. Liang, Z. Liu, S. Zhang, B. Huang, Intravoxel incoherent motion (IVIM) in evaluation of breast lesions: comparison with conventional DWI, European journal of radiology 82 (12) (2013) e782–e789.
- [20] S. Goshima, M. Kanematsu, Y. Noda, H. Kondo, H. Watanabe, K.T. Bae, Diffusion kurtosis imaging to assess response to treatment in hypervascular hepatocellular carcinoma, Am. J. Roentgenol. 204 (5) (2015) W543–W549, <https://doi.org/10.2214/AJR.14.13235>.
- [21] S. van Baalen, A. Leemans, P. Dik, M.R. Lilien, B. ten Haken, M. Froeling, Intravoxel incoherent motion modeling in the kidneys: comparison of mono-, bi-, and triexponential fit, J. Magn. Reson. Imag. 46 (1) (2017) 228–239, <https://doi.org/10.1002/jmri.25519>.
- [22] R. Wu, S.T. Suo, L.M. Wu, Q.Y. Yao, H.X. Gong, J.R. Xu, Assessment of chemotherapy response in non-Hodgkin lymphoma involving the neck utilizing diffusion kurtosis imaging: a preliminary study, Diagn. Interventional Radiol. 23 (3) (2017) 245–249, <https://doi.org/10.5152/dir.2017.16184>. Apr.
- [23] M. Beyhan, R. Sade, E. Koc, S. Adanur, M. Kantarcı, The evaluation of prostate lesions with IVIM DWI and MR perfusion parameters at 3T MRI, La radiologia medica 124 (2) (2019) 87–93.
- [24] A. Lecler, et al., Intravoxel incoherent motion (IVIM) 3 T MRI for orbital lesion characterization, Eur. Radiol. 31 (1) (Jan. 2021) 14–23, <https://doi.org/10.1007/s00330-020-07103-1>.
- [25] N. Fujima, et al., Prediction of the treatment outcome using intravoxel incoherent motion and diffusional kurtosis imaging in nasal or sinonasal squamous cell carcinoma patients, Eur. Radiol. 27 (3) (2017) 956–965, <https://doi.org/10.1007/s00330-016-4440-1>. Mar.
- [26] N.D. Sijtsma, et al., An optimal acquisition and post-processing pipeline for hybrid IVIM-DKI in head and neck, Magn. Reson. Med. (2020), <https://doi.org/10.1002/mrm.28461>.
- [27] N. Just, Improving tumour heterogeneity MRI assessment with histograms, Br. J. Cancer 111 (12) (Dec. 2014), <https://doi.org/10.1038/bjc.2014.512>. Art. no. 12.
- [28] M. Styner, C. Brechbuhler, G. Szekely, G. Gerig, Parametric estimate of intensity inhomogeneities applied to MRI, IEEE Trans. Med. Imag. 19 (3) (2000) 153–165.
- [29] L.I. Rudin, S. Osher, E. Fatemi, Nonlinear total variation based noise removal algorithms, Phys. Nonlinear Phenom. 60 (1) (1992) 259–268, [https://doi.org/10.1016/0167-2789\(92\)90242-F](https://doi.org/10.1016/0167-2789(92)90242-F). Nov.
- [30] K. Holzapfel, S. Duettsch, C. Fauser, M. Eiber, E.J. Rummey, J. Gaa, Value of diffusion-weighted MR imaging in the differentiation between benign and malignant cervical lymph nodes, Eur. J. Radiol. 72 (3) (Dec. 2009) 381–387, <https://doi.org/10.1016/j.ejrad.2008.09.034>.
- [31] L.-P. Qi, et al., Discrimination of malignant versus benign mediastinal lymph nodes using diffusion MRI with an IVIM model, European Radiology 2017 28:3 28 (3) (2017) 1301–1309, <https://doi.org/10.1007/s00330-017-5049-8>. Sep.
- [32] Y. Cui, et al., Differentiation of prostate cancer and benign prostatic hyperplasia: comparisons of the histogram analysis of intravoxel incoherent motion and monoexponential model with in-bore MR-guided biopsy as pathological reference, Abdominal Radiology (2019) 1–13.
- [33] Y. Ding, et al., Differentiating between malignant and benign renal tumors: do IVIM and diffusion kurtosis imaging perform better than DWI? Eur. Radiol. 29 (12) (2019) 6930–6939, <https://doi.org/10.1007/s00330-019-06240-6>. Dec.
- [34] W. Junping, S. Tongguo, Z. Yunting, Y. Chunshui, B. Renju, Discrimination of axillary metastatic from nonmetastatic lymph nodes with PROPELLER diffusion-weighted MR imaging in a metastatic breast cancer model and its correlation with cellularity, J. Magn. Reson. Imag. 36 (3) (2012) 624–631, <https://doi.org/10.1002/jmri.23695>.
- [35] A. Perrone, et al., Diffusion-weighted MRI in cervical lymph nodes: differentiation between benign and malignant lesions, Eur. J. Radiol. 77 (2) (Feb. 2011) 281–286, <https://doi.org/10.1016/j.ejrad.2009.07.039>.
- [36] D. Le Bihan, E. Breton, D. Lallemand, M.L. Aubin, J. Vignaud, M. Laval-Jeantet, Separation of diffusion and perfusion in intravoxel incoherent motion MR imaging, Radiology 168 (2) (1988) 497–505.

- [37] J. Yu, et al., Diffusion kurtosis imaging in identifying the malignancy of lymph nodes during the primary staging of rectal cancer, *Colorectal Dis.* 20 (2) (2018) 116–125, <https://doi.org/10.1111/codi.13835>.
- [38] Y. Liu, et al., The diagnostic accuracy of intravoxel incoherent motion and diffusion kurtosis imaging in the differentiation of malignant and benign soft-tissue masses: which is better? *Acta Radiol* 63 (6) (Jun. 2022) 785–793, <https://doi.org/10.1177/02841851211017511>.
- [39] Y. Huang, et al., Diffusion kurtosis at 3.0T as an in vivo imaging marker for breast cancer characterization: correlation with prognostic factors, *J. Magn. Reson. Imag.* 49 (3) (2019) 845–856, <https://doi.org/10.1002/jmri.26249>.
- [40] N. Dikaios, et al., Logistic regression model for diagnosis of transition zone prostate cancer on multi-parametric MRI, *Eur. Radiol.* 25 (2) (2015) 523–532, <https://doi.org/10.1007/s00330-014-3386-4>. Feb.
- [41] B. Wang, et al., Value of magnetic resonance imaging texture analysis in the differential diagnosis of benign and malignant breast tumors, *Chin. Med. Sci. J.* 34 (1) (2019) 33–37, <https://doi.org/10.24920/003516>. Mar.
- [42] W. Sun, et al., A CT-based radiomics nomogram for distinguishing between benign and malignant bone tumours, *Cancer Imag.* 21 (1) (2021) 20, <https://doi.org/10.1186/s40644-021-00387-6>. Feb.
- [43] Y.Y. Sabri, N.M. Ewiss, H.E.H. Zawam, M.A. Khairy, Role of diffusion MRI in diagnosis of mediastinal lymphoma: initial assessment and response to therapy, *Egypt J Radiol Nucl Med* 52 (1) (2021) 215, <https://doi.org/10.1186/s43055-021-00597-9>. Aug.
- [44] X.-P. Yu, et al., Intravoxel incoherent motion diffusion weighted magnetic resonance imaging for differentiation between nasopharyngeal carcinoma and lymphoma at the primary site, *J. Comput. Assist. Tomogr.* 40 (3) (Jun. 2016) 413–418, <https://doi.org/10.1097/RCT.0000000000000391>.
- [45] Y. Cheng, et al., Preliminary clinical results for PET/MR compared with PET/CT in patients with nasopharyngeal carcinoma, *Oncol. Rep.* 43 (1) (Jan. 2020) 177–187, <https://doi.org/10.3892/or.2019.7392>.
- [46] H.M. Bülbül, O. Bülbül, S. Sarıoğlu, Ö. Özdogan, E. Doğan, N. Karabay, Relationships between DCE-MRI, DWI, and 18F-FDG PET/CT parameters with tumor grade and stage in patients with head and neck squamous cell carcinoma, *Mol Imaging Radionucl Ther* 30 (3) (Oct. 2021) 177–186, <https://doi.org/10.4274/mirt.galenos.2021.25633>.
- [47] C.J. Tyng, et al., Correlation of the ADC values assessed by diffusion-weighted MRI and 18F-FDG PET/CT SUV in patients with lung cancer, *Applied Cancer Research* 38 (1) (2018) 9, <https://doi.org/10.1186/s41241-018-0060-1>. Apr.
- [48] Z. Li-Ou, et al., Correlation between tumor glucose metabolism and multiparametric functional MRI (IVIM and R2*) metrics in cervical carcinoma: evidence from integrated 18F-FDG PET/MR, *J. Magn. Reson. Imag.* 49 (6) (2019) 1704–1712, <https://doi.org/10.1002/jmri.26557>.
- [49] R. Azadnia, S. Fouladi, A. Jahanbakhshi, Intelligent detection and waste control of hawthorn fruit based on ripening level using machine vision system and deep learning techniques, *Results in Engineering* 17 (2023) 100891, <https://doi.org/10.1016/j.rineng.2023.100891>. Mar.
- [50] W.A. Khan, F. Sultan, M. Ali, M. Shahzad, M. Khan, M. Irfan, Consequences of activation energy and binary chemical reaction for 3D flow of Cross-nanofluid with radiative heat transfer, *J. Braz. Soc. Mech. Sci. Eng.* 41 (1) (2018) 4, <https://doi.org/10.1007/s40430-018-1482-0>. Nov.
- [51] W.A. Khan, M. Ali, F. Sultan, M. Shahzad, M. Khan, M. Irfan, Numerical interpretation of autocatalysis chemical reaction for nonlinear radiative 3D flow of cross magnetofluid, *Pramana - J. Phys.* 92 (2) (2019) 16, <https://doi.org/10.1007/s12043-018-1678-y>. Jan.